Article

Quantification of CH$_4$ Hydrate Film Growth Rates in Micromodel Pores

Stian Almenningen,* Maksim Lysyy, and Geir Ersland

ACCESS | Metrics & More | Article Recommendations

ABSTRACT: In this paper, we report the growth pattern and the rate of CH$_4$ hydrate in sandstone pores. A high-pressure, water-wet, transparent micromodel with pores resembling a sandstone rock was used to visualize CH$_4$ hydrate formation at reservoir conditions (P = 35−115 bar and T = 0.1−4.9 °C). The CH$_4$ hydrate preferably formed and grew along the gas−water interface until the gas phase was completely encapsulated by a hydrate film. Two different growth rates were identified on the gas−water interface: CH$_4$ hydrate film growth along the vertical pore walls (∼1200 μm/s) was more than 100 times faster than the film growth toward the pore center (∼8 μm/s). CH$_4$ hydrate crystal growth directly in the water phase was slow and the rate was less than 0.5 μm/s. The film growth rate along the gas−water interface was independent of the pore size, gas saturation, and gas distribution, but the pore wall growth rate displayed a power law dependency on the applied subcooling temperature, ΔT, with a power law exponent equal to 2. The results of this study can be used as input to numerical models aiming to simulate pore-scale CH$_4$ hydrate growth behavior.

Quantification of CH$_4$ hydrate growth rates in porous media
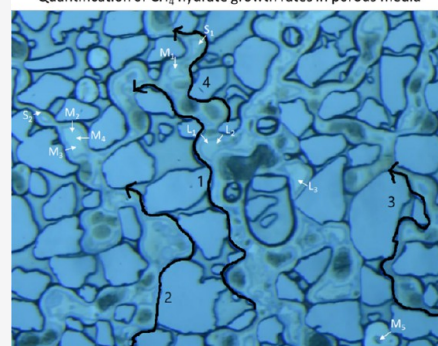
1. INTRODUCTION

Natural gas hydrates are solid inclusion compounds consisting of crystalline water and one or more guest molecules. Gas hydrates were first perceived as a nuisance by the oil and gas industry, but later, gas hydrates were recognized as a tremendous source of subsurface methane (CH$_4$) gas. The estimated reserves of CH$_4$ gas trapped in gas hydrates are compared to the known reserves of conventional fossil energy resources.[1] Extensive research in the last decades has therefore been devoted to enable safe and economically viable production of CH$_4$ gas from hydrate-bearing sediments. Still, the fundamental nature of CH$_4$ hydrate growth in a porous medium is not clear. The rate at which the hydrate grows, both on the gas−water interface and in liquid water containing dissolved CH$_4$, is an important parameter that is needed to accurately model the formation of hydrate accumulations in natural geological settings. The rate at which the hydrate dissociates is closely linked to how the hydrate was formed and how the hydrate and related fluids are distributed in a porous medium.[2] Understanding the pore-scale growth pattern of gas hydrates is therefore vital for assessing and predicting CH$_4$ gas production from natural sediments and the stability of hydrates in the context of climate change.

Hydrate film growth at various gas−water interfaces has been extensively studied in bulk systems.[3−8] The growth rate of the CH$_4$ hydrate along a planar gas−water interface was increased with the degree of subcooling, and the hydrate film thickness increased with time and the degree of subcooling.[3] The hydrate growth rate was also sensitive to which hydrate

former was being used; the CO$_2$ hydrate grew faster than the CH$_4$ hydrate, which again grew faster than the propane hydrate.[4] This was ascribed to the guest molecule's ability to dissolve in liquid water, and similarly, the hydrate film thickness was dependent on the type of the guest molecule.[3] The degree of subcooling is also known to affect the hydrate crystal morphology.[7] Servio and Englezos[9] suggested that the growth of dendritic hydrate crystals at high driving forces is due to a larger number of nucleation sites compared to that at low driving forces. However, the thermodynamic properties in a porous medium are different from those in bulk systems due to molecular interactions between the hydrophilic mineral surfaces and the fluids and the energy necessary to support capillary equilibrium.[10] In this paper, the CH$_4$ hydrate growth pattern and rate are described and quantified in sandstone pores using a high-pressure transparent micromodel. The paper builds on a hydrate growth rate quantification technique that was introduced by Hauge et al.[11] and later used by Muraoka and Yamamoto.[12] Two different hydrate growth rates were identified in those studies: hydrate growth parallel to the grains was 2 orders of magnitude higher than hydrate growth
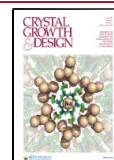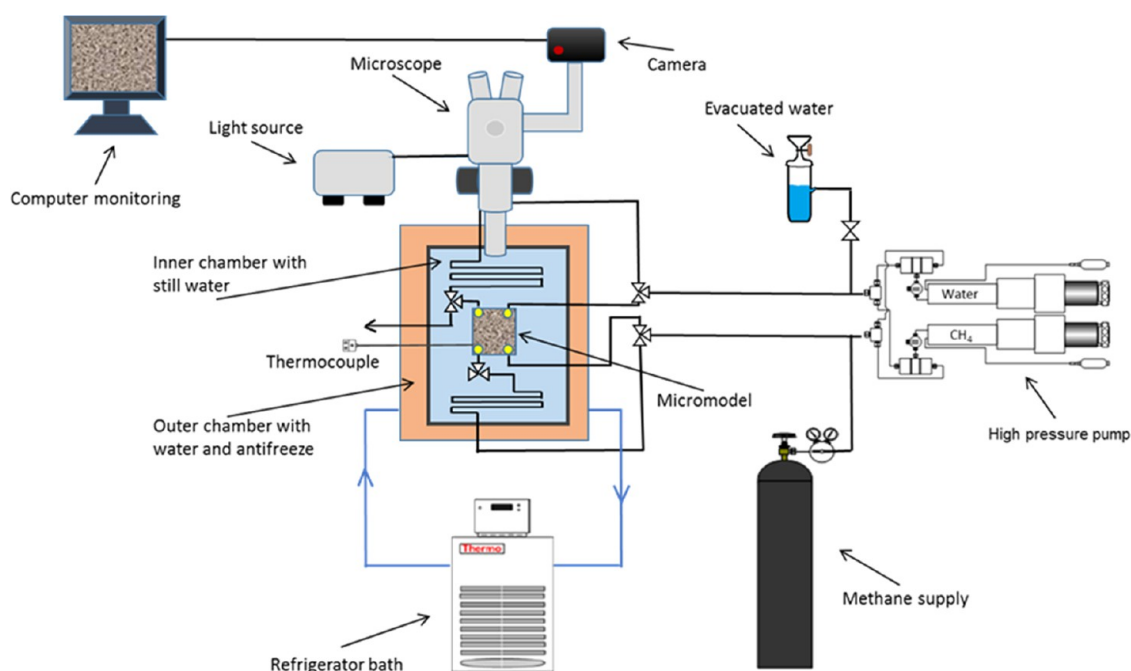
Figure 1. Overview of experimental setup including the micromodel, the high-pressure pump for injection and production of fluids, the refrigerator bath for controlling the temperature, the microscope, and the camera for recording images of hydrate growth in the pore space.

toward the pore centers.[12] This paper extends the previous work on hydrate growth rates in micromodels and includes the effect of pore size, gas saturation, gas distribution, and degree of subcooling on the CH_4 hydrate film growth rate.

2. MATERIALS AND METHODS

2.1. Experimental Setup. The micromodel consisted of a transparent glass plate glued together with a silicon wafer through anodic bonding. A pore network replicating Berea sandstone was etched into the silicon wafer through the deep reactive ion-etching technique.[13] The average pore diameter was on the order of 100 μm, and the pore height was constant, equal to 25 μm. The total width and length of the pore network were approximately 2.2 and 2.8 cm, respectively. The anodic bonding technique resulted in a water-wet model in which the gas occupied the center of the pores and water coated the silicon grains and the glass plate. A steel casing was used as a confinement, and the mounted model was submerged in still water for temperature control (Figure 1). A constant temperature was applied by circulation (Thermo Neslab RTE 17) of antifreeze through a separate outer chamber adjacent to the still water in the inner chamber. The system temperature was measured by a thermocouple (Omega thermocouple type T) placed in the still water directly beneath the micromodel. A high-pressure pump (Quizix Q5200) was connected to opposite corners of the micromodel through polyetheretherketone (PEEK) capillary tubing. One pump cylinder was filled with methane gas (>99.5%), and the other pump cylinder was filled with distilled water. Still pictures and a video of the pore space were recorded by a camera (Nikon D7100) connected to a microscope (Nikon SMZ 1500) situated above the micromodel. The working distance was 54 mm, and the field of view (FOV) was in the order of 2 mm using 1× objective lenses and a 110× magnification.

2.2. Experimental Procedure. The model was cleaned with water prior to each experiment and then saturated with a given amount of CH_4 gas by gas injection. The water pump was disconnected from the model, and the pore pressure was maintained by a gas pump. The model was pressurized with gas and water in the pore space for several hours to saturate the water with CH_4 and to check for leakages. Hydrate formation was initiated by decreasing the temperature, and hydrate growth commenced and continued with constant pore pressure and temperature. Different initial saturations

and different pressures and temperatures were used for experiments to investigate the effect on the hydrate growth rate. The hydrate growth rate (μm/s) was quantified by measuring the hydrate film length versus time. The growth rate was then given as the slope of the best-fit linear trend line. Multiple measurements of the growth rate were conducted in different pores for each experiment to produce a representative growth rate for each experimental condition.

3. RESULTS AND DISCUSSION

A total of 20 CH_4 hydrate formation experiments were conducted to reveal the nature of hydrate growth in the micromodel and to quantify the hydrate growth rates. The

Table 1. Overview of Experimental Conditions for Each Experiment

| exp.	P (bar)	T (°C)	S_{gi} (frac.)
1	83.0	1.2	0.27
2	83.0	1.3	0.51
3	84.0	1.3	0.30
4	83.0	1.2	0.50
4.1	59.2	1.1	~0.5
5	83.0	1.4	0.39
6	83.0	1.3	0.36
7	83.0	1.3	0.52
7.1	38.4	1.3	~0.5
7.2	77.0	1.3	~0.5
8	115.0	4.9	~0.5
8.1	40.0	0.1	~0.5
8.2	35.0	0.6	~0.5
9	57.5	1.4	~0.5
10	45.9	1.5	~0.5
11	46.0	1.6	~0.5
12	42.0	1.5	~0.5
13	52.0	1.5	~0.5
14	67.0	1.5	~0.5
15	100.0	1.5	~0.5
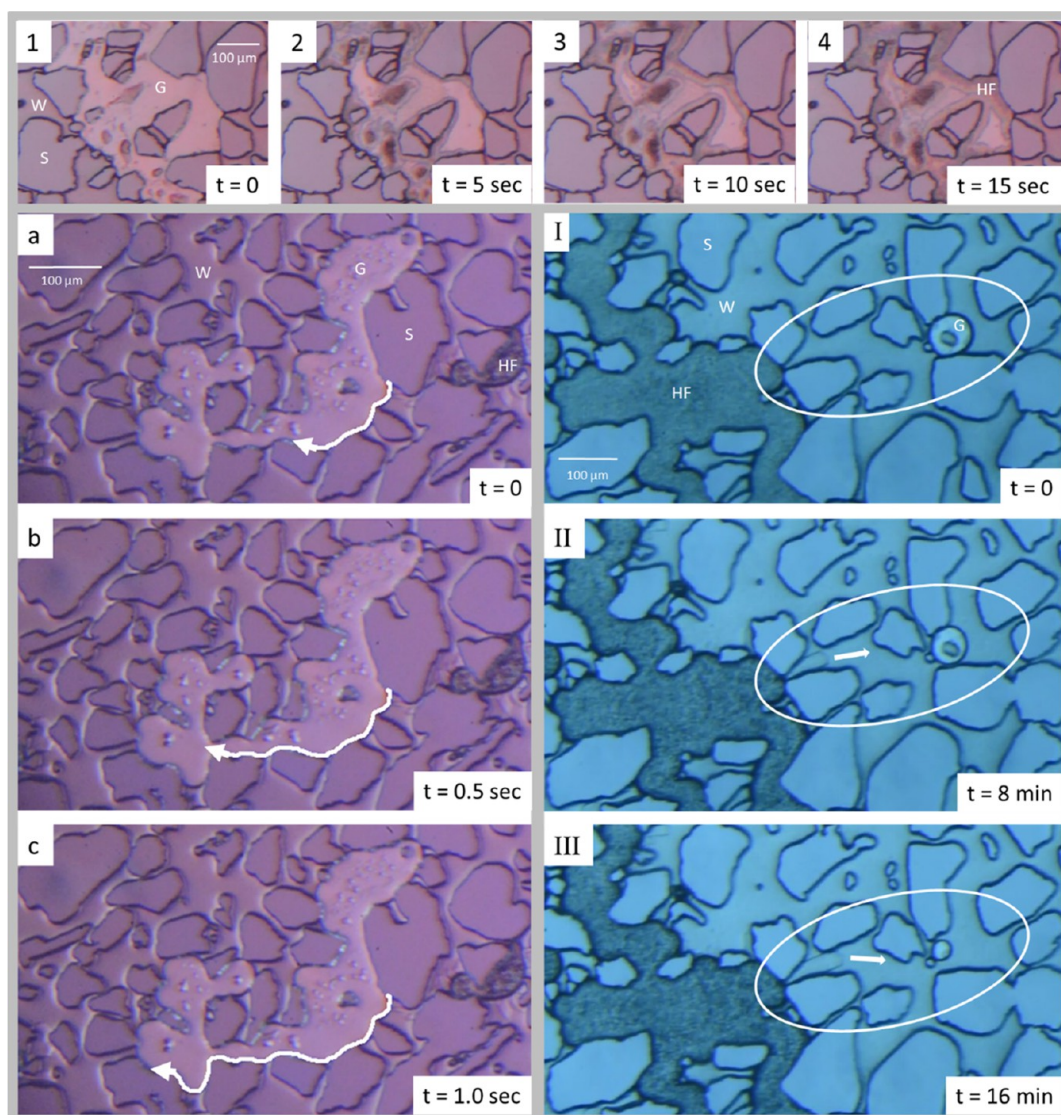
Figure 2. Overview of three different hydrate growth patterns observed in this study. (1−4) Pore center hydrate growth at P = 83 bar and T = 1.1 °C. (a−c) Pore wall hydrate growth at P = 83 bar and T = 1.2 °C. (I−III) Hydrate crystal growth in the water phase at P = 84 bar and T = 1.3 °C. S is sediment, W is water, G is gas, and HF is the hydrate film.

hydrate formation pressure ranged between 35 and 115 bar in experiments, and the temperature ranged between 0.1 and 4.9 °C (Table 1). The initial gas saturation in the field of view (FOV) varied between 0.27 and 0.52 frac. to investigate the effect of initial gas saturation on the hydrate growth rates. The first part of this section explores the different hydrate growth patterns that were observed during the hydrate formation, while the second part is devoted to quantifying the hydrate growth rates.

3.1. Hydrate Growth Patterns. Hydrate nucleation typically occurred on the gas−water interface and was followed by a hydrate film spreading along the gas−water interface. The exact location of the first hydrate nucleation and the number of nucleation points could not be determined using the given experimental apparatus. However, once the initial hydrate film was observed, it spread quickly along the vertical gas−water interface, as observed in Figure 2a−c. The hydrate film is here tracked during the first second of growth and is shown by a white arrow. Hydrate film growth along the vertical gas−water interface is labeled as the pore wall hydrate growth rate, v_w,

throughout the manuscript. The pore wall hydrate growth was followed by a slower hydrate growth along the gas−water interface toward the pore center. This growth mechanism is exemplified in Figure 2(1−4). A thin water film always wetted the glass plate on the top of the pores because of the water-wet nature of the micromodel and hydrate grew along the interface between the water film and the nonwetting gas phase that was saturating the pores. Hydrate film growth toward the pore center is from now on labeled as the pore center hydrate growth rate, v_c.

The pore center hydrate growth eventually led to a complete encapsulation of the gas phase. From there, two different scenarios could evolve as observed and described by Almenningen et al.[14] and Pandey et al.[15] The gas phase was usually fully consumed by hydrate growth in areas with low-to-moderate gas saturation, whereas gas remained coated by a hydrate film in areas with high gas saturation and limited availability of water. The mechanism behind full consumption of the gas phase/gas bubbles was not clear but was investigated further by analyzing the change in pixel intensity of the hydrate
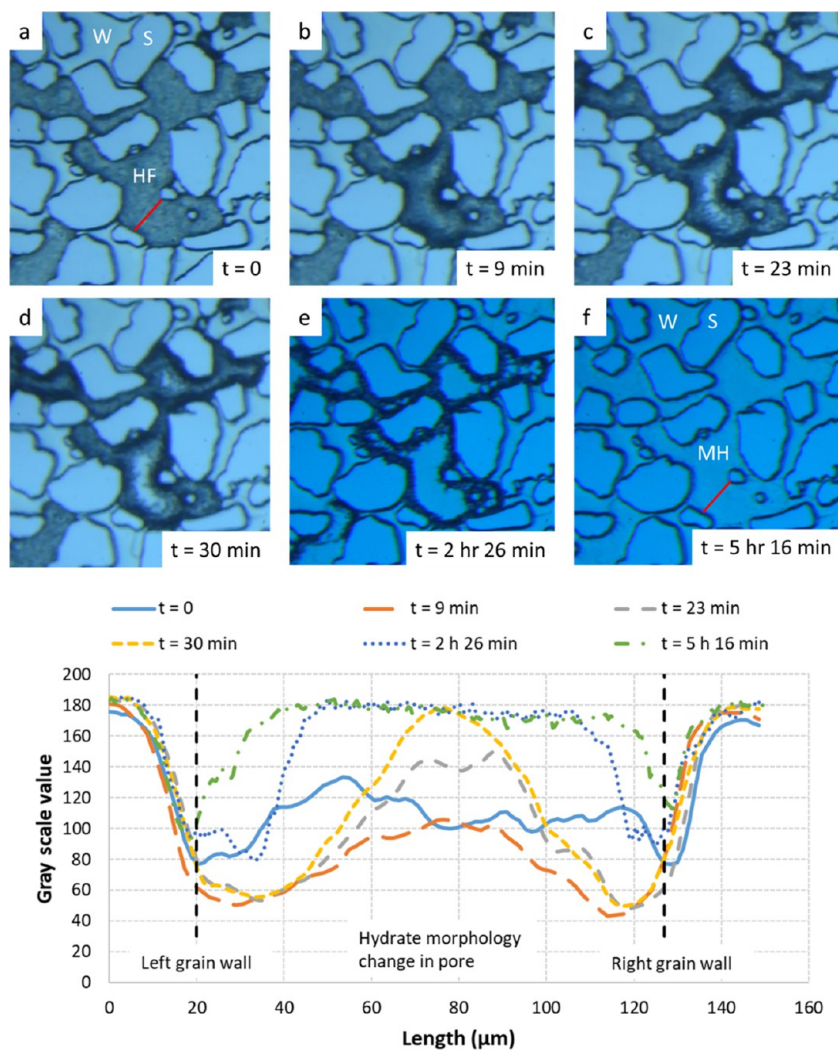
Figure 3. Upper: Hydrate growth sequence at $P = 83$ bar and $T = 1.3$ °C. (a) Pore space is mainly saturated by a gas phase encapsulated by a hydrate film and some liquid water. (b−f) Gas is consumed as the hydrate film continues to grow until the pore space is saturated by a massive hydrate phase without any gas. S is sediment, W is water, HF is the hydrate film, and MH is massive hydrate. Lower: Grayscale intensity values along the line segment marked by the red line in the upper figure. The time steps in the graph correspond to the images presented in the upper figure.
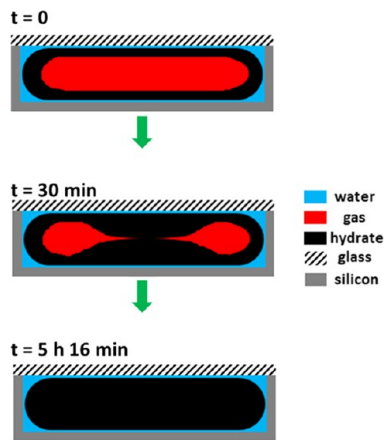

Figure 4. Conceptual model of gas consumption during hydrate growth in a pore initially saturated by gas coated by a hydrate film. The model is based on the observations presented in Figure 3.

phase during the transition from porous hydrate to nonporous massive hydrate (Figure 3). Figure 3 a shows a gas phase that

was already encapsulated by a hydrate film. The additional images display the gradual transition in areas where the gas phase was fully consumed. Notice that complete consumption of the gas occurred first in the largest pores (Figure 3c−e) and later in the smaller pores. Eventually, all of the pores were saturated with 100% massive hydrate after approximately 5 h of hydrate growth (Figure 3f).

The change in the pixel intensity of the line segment spanning across the pore is shown for the same time steps in the lower part of Figure 3. At time zero, the grayscale intensity was nearly constant across the pore, indicating a hydrate film with nearly constant thickness. During the next 30 min, the grayscale intensity decreased slightly close to the grain walls, whereas it increased in the middle of the pore. The increase of the grayscale intensity meant that the gas was consumed and that a solid hydrate phase developed, spanning from top to bottom in the middle of the pore (Figure 4). The correlation between the grayscale intensity and the hydrate morphology is explained in detail by Almenningen et al.[16] The grayscale intensity increased closer to the pore walls as the hydrate growth continued, and after approximately 5 h, the grayscale
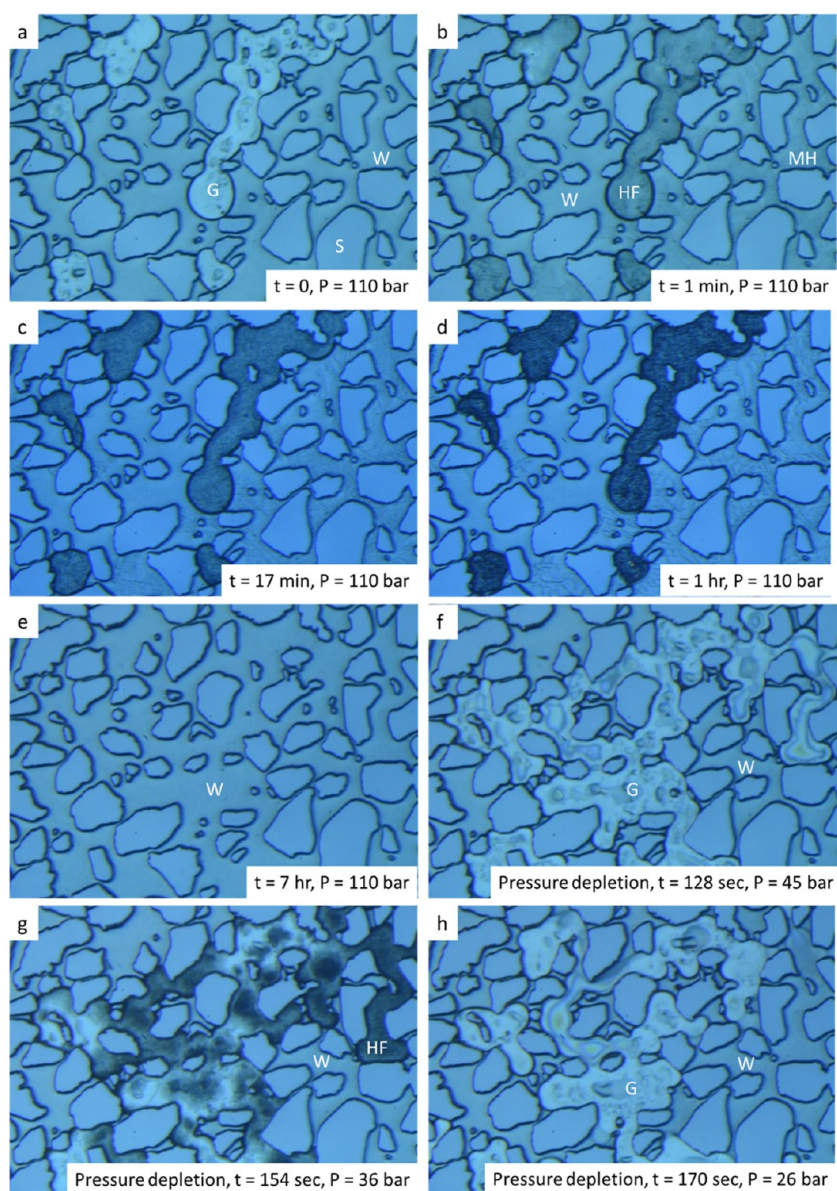
Figure 5. Hydrate growth and dissociation sequence at constant $T = 0.1$ °C. (a−d) Hydrate film encapsulates the gas phase, and more than half of the water phase crystallizes into massive hydrate. (e) All of the hydrates dissociate, and the gas dissolves in the water phase. (f) Pressure is rapidly decreased, and the gas phase reappears at $P = 45$ bar. (g) Hydrate film evolves and encapsulates the gas phase upon continued pressure depletion. (h) Hydrate film dissociates as the pressure is lowered below the hydrate stability pressure. S is sediment, W is water, G is the gas, HF is the hydrate film, and MH is massive hydrate.

intensity was nearly constant across the entire length of the pore, which corresponded to the complete formation of massive hydrate in the pore. The pixel intensity analysis therefore revealed that the gas was first consumed in the middle of the pore and later close to the pore walls (Figure 4). The reason for this particular growth pattern is not clear, but likely involves the continuous dissociation and reformation of hydrate crystals known as Ostwald ripening.[17]

Hydrate crystal growth directly in the water phase was observed in some cases and was usually triggered by high thermodynamic driving forces. In a few rare cases, hydrate was observed to grow from a hydrate-coated gas phase via the water phase toward other gas bubbles that were not already covered by hydrate films. This growth pattern is highlighted in Figure 2(I−III). Here, a hydrate front emerged in the water phase adjacent to a gas phase covered by a hydrate film and

started to grow toward an isolated gas bubble residing around 200 μm away from the hydrate-covered gas phase (Figure 2(I)). The gas bubble shrank in size as the hydrate front advanced toward it (Figure 2(II,III)), and the gas bubble was likely feeding gas through liquid diffusion to the approaching hydrate front. The hydrate crystal seized to grow in the water phase exactly as the gas bubble was fully consumed, and consequently, there was no gas left to fuel the hydrate growth. In another similar case, the isolated gas bubble was large enough to sustain hydrate growth in the water phase until the hydrate crystal reached all the way to the gas bubble. The gas bubble was then immediately covered by a hydrate film, which was later fully consumed by hydrate growth. The directional growth of the hydrate in the water phase along concentration gradients of dissolved CH_4 is probably an example of one of
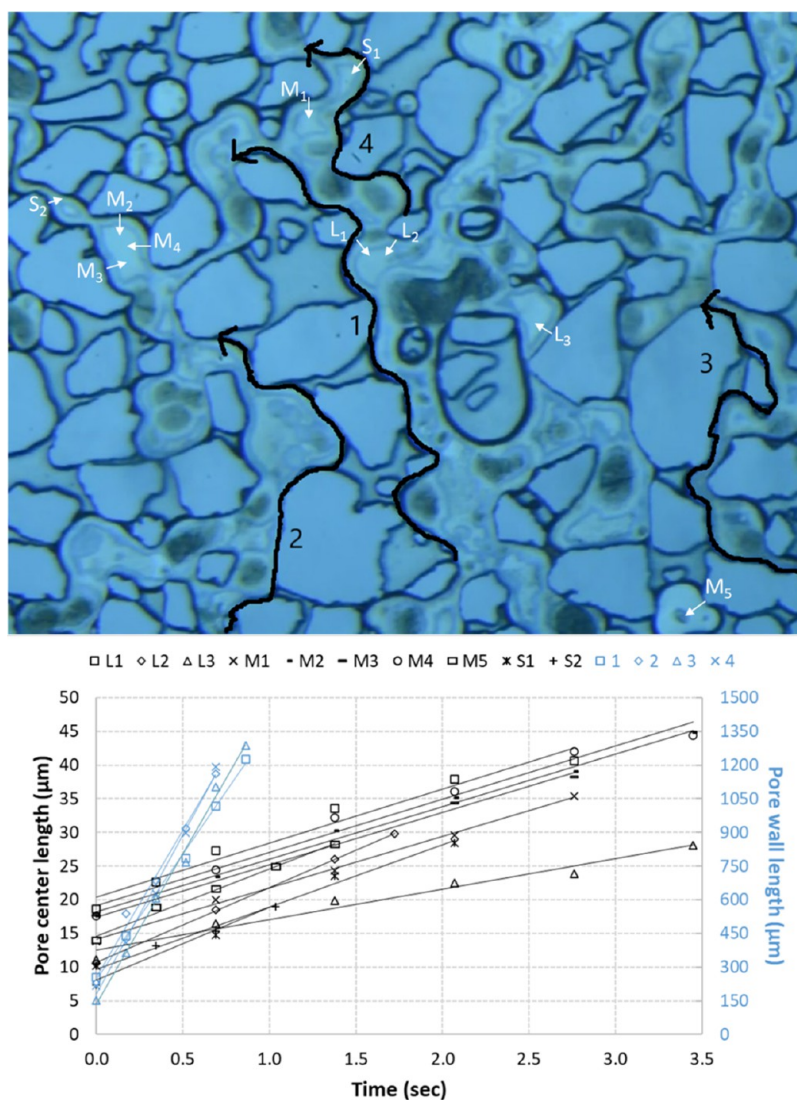
Figure 6. Upper: Overview of where hydrate growth rates were calculated in Exp. 4. Four pore wall growth rates (1−4) and 10 pore center growth rates were calculated. The pore center growth rates were located in large (L_1−L_3), medium (M_1−M_5), and small (S_1−S_2) pores. Lower: Development of the hydrate film length as a function of time.

the growth patterns occurring in nature in water supersaturated by the CH_4 gas.

The hydrate growth rate in water was much slower than the growth rate along the gas−water interface and will be discussed in the next section. However, another growth mechanism was observed in the water phase when high thermodynamic driving forces were applied and when the hydrate formation was a secondary formation. A large part of the water phase crystallized into hydrate within seconds without any clear growth direction. This is seen in Figure 5, where the gas phase was covered by a hydrate film and a large part of the water phase crystallized into massive hydrate. The hydrate film initially increased in thickness with time, and the hydrate crystals in the water phase grew to become more distinct (Figure 5a−d). Then, during the next hours, all of the hydrates dissociated, and the gas phase vanished completely in the FOV (Figure 5e). The shock-induced hydrate formation at high driving forces was clearly not thermodynamically stable, and the water phase was likely undersaturated with the CH_4 gas in other parts of the micromodel. This induced hydrate dissociation through CH_4 dissolution in the water phase.

The pore pressure was then quickly reduced, and the gas phase reappeared at a pressure of 45 bar in response to the lower solubility of CH_4 in water with decreasing pressure (Figure 5f). The pressure was still above the hydrate formation pressure (P_{eq} = 26.2 bar at T = 0.1 °C) and a hydrate film developed in the gas phase as the pressure reduction continued. Figure 5g shows a snapshot of the evolving hydrate film as the pressure was lowered to 36 bar. If the pressure reduction was stopped now, the hydrate formation could have continued, and a stable hydrate phase would have formed. Instead, the pressure was lowered further below the hydrate stability pressure and the newly formed hydrate film dissociated accordingly (Figure 5h). This experiment demonstrated the possibility of forming hydrates in water undersaturated with the CH_4 gas by rapidly decreasing the pore pressure and that this may be an effective technique for forming hydrates in the laboratory.

3.2. Hydrate Growth Rates. The hydrate growth rates were divided into two different types based on the observations of hydrate growth patterns in the previous section. The pore center growth rate, v_c, was measured normal to the pore wall and toward the pore center, while the pore wall growth rate, v_w,

Table 2. Hydrate Growth Rates in Exp. 4[a]

	pore center growth			pore wall growth		
location	v_c (μm/s)	R^2	location	v_w (μm/s)	R^2	
L1	8.0	0.96	1	1117	1.00	
L2	11.1	1.00	2	1303	0.99	
L3	4.5	0.97	3	1336	0.99	
average large	7.9 ± 3.3		4	1417	0.99	
M1	7.6	1.00				
M2	7.8	0.99				
M3	7.8	0.99				
M4	7.9	0.98				
M5	10.0	0.99				
average medium	8.2 ± 1.0					
S1	6.3	0.98				
S2	10.8	0.97				
average small	8.6 ± 3.2					
average total	8 ± 2			1290 ± 130		

[a]The growth rates in each location correspond to the slope of the linear trend lines in Figure 4. The uncertainty of the average growth rate is calculated as the standard deviation.

Table 3. Pore Center Hydrate Growth Rates for Each Pore Size in Each Experiment[a]

	pore center growth			
Exp.	pore size	v_c (μm/s)	±Δv (μm/s)	n
1	medium	2.7	0.9	4
	large	3.2	0.7	3
	average	2.9	0.8	7
2	small	2.5	0.9	3
	medium	2.1	0.8	3
	large	1.7	1.0	3
	average	2.1	0.9	9
3	small	13.5	1.3	3
	medium	14.2	2.0	4
	large	15.4	3.8	4
	average	14.4	2.5	11
4	small	8.6	2.3	2
	medium	8.2	1.0	5
	large	7.9	3.3	3
	average	8.2	2.0	10
5	small	7.2	1.4	3
	medium	6.8	2.2	5
	large	4.9	1.0	3
	average	6.4	1.9	11
6	small	8.0	1.5	4
	medium	6.1	1.4	3
	large	5.6	2.8	3
	average	6.7	2.0	10
7	small	10.0	2.1	5
	medium	10.5	1.5	5
	average	10.3	1.8	10
	average total	8	4	125

[a]The pressure was 83−84 bar and the temperature was 1.2−1.4 °C. The uncertainty, Δv, is calculated as the standard deviation of the measurements, and n is the total number of measurements.

was measured parallel to the pore wall. Several measurements of each growth rate were obtained for each experiment as exemplified for Exp. 4 in Figure 6. Each growth rate was calculated by implementing a best-fit linear trend line through the data points representing length versus time (Figure 6). The
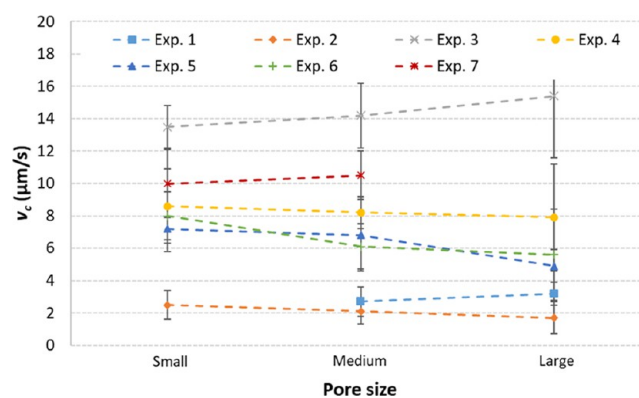

Figure 7. Pore center hydrate growth rates for each pore size in each experiment. The uncertainty, Δv, is calculated as the standard deviation of the measurements.

Table 4. Pore Center Growth Rates and Pore Wall Growth Rates for Each Experiment

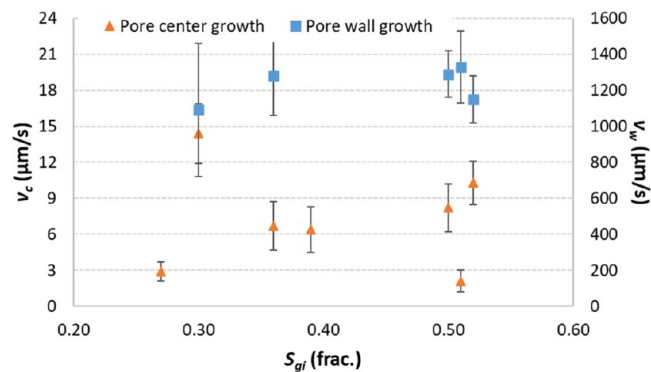| Exp.	S_{gi} (frac.)	pore center growth			pore wall growth		
		v_c (μm/s)	±Δv (μm/s)	n	v_w (μm/s)	±Δv (μm/s)	n
1	0.27	2.9	0.8	7			
2	0.51	2.1	0.9	9	1330	200	3
3	0.30	14.4	2.5	11	1090	370	4
4	0.50	8.2	2.0	10	1290	130	4
5	0.39	6.4	1.9	11			
6	0.36	6.7	2.0	10	1280	220	3
7	0.52	10.3	1.8	10	1150	130	3

Figure 8. Hydrate growth rates for each experiment as a function of initial gas saturation. The pore center growth rates are displayed in orange diamonds on the left vertical axis, and the pore wall growth rates are displayed in blue squares on the right vertical axis.

pore center growth rates were also grouped according to the pore size in which the rate was measured. All measurements of pore center and pore wall growth rates in Exp. 4 are detailed in Table 2.

3.2.1. Effect of the Pore Size. The pore center growth rate was measured 2−5 times for each pore size in each experiment (Table 3). The pore size was categorized as small (<80 μm), medium (80−180 μm), and large (>180 μm). Each experiment (1−7) was conducted at a pressure of 83−84 bar and a temperature of 1.2−1.4 °C. The pore wall growth rate was usually measured across several pores and could not be linked to specific pore sizes.

The results showed no significant correlation between the pore size and the pore center growth rate (Figure 7). There

Table 5. Pore Center Growth Rates in the Continuous Gas and the Isolated Gas for Each Experiment

	pore center growth		
Exp.	gas distribution	v_c (μm/s)	$\pm\Delta v$ (μm/s)
1	continuous		
	isolated	2.9	0.8
2	continuous	2.0	1.0
	isolated	1.7	0.4
3	continuous	13.7	2.4
	isolated	16.7	1.5
4	continuous	8.0	2.0
	isolated	10.0	
5	continuous	5.8	1.4
	isolated	9.2	0.1
6	continuous	7.1	1.6
	isolated	5.9	3.0
7	continuous	10.3	1.8
	isolated		
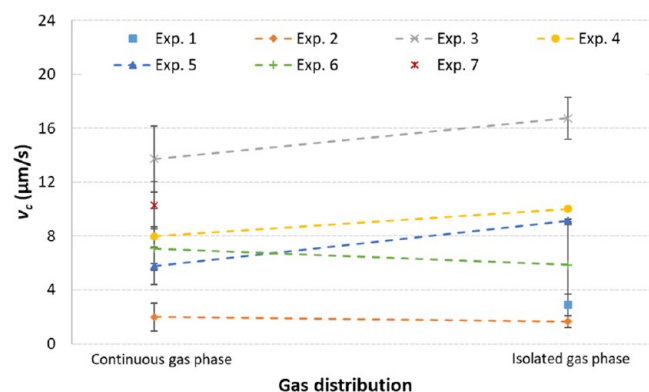
Figure 9. Pore center growth rates in the continuous gas and the isolated gas for each experiment.

Table 6. Hydrate Growth Rates for Each Experiment[a]

			pore center growth			pore wall growth		
Exp.	ΔP (bar)	ΔT (°C)	v_c (μm/s)	$\pm\Delta v$ (μm/s)	n	v_w (μm/s)	$\pm\Delta v$ (μm/s)	n
1	53.6	10.1	2.9	0.8	7			
2	53.3	10.0	2.1	0.9	9	1330	200	3
3	54.3	10.2	14.4	2.5	11	1090	370	4
4	53.6	10.1	8.2	2.0	10	1290	130	4
4.1	30.2	7.1	8.2	3.6	7	570	50	3
5	52.9	9.9	6.4	1.9	11			
6	53.3	10.0	6.7	2.0	10	1280	220	3
7	53.3	10.0	10.3	1.8	10	1150	130	3
7.1	8.7	2.5				100	10	3
7.2	47.3	9.0	11.4	2.6	15	1020	220	3
8	72.5	9.2	8.5	2.2	13			
8.1	13.8	4.2	2.8	1.3	12	190	40	3
8.2	7.5	2.4	1.8	0.7	10	80	15	5
9	27.4	6.4	3.5	1.9	7	450	40	3
10	15.5	4.2	1.7	0.7	7	220	20	5
11	15.3	4.1	1.7	0.5	7	180	10	5
12	11.6	3.3	1.2	0.4	7	100	20	5
13	21.6	5.4	1.5	0.7	7	270	10	5
14	36.6	7.8	2.7	1.0	8	590	60	5
15	69.6	11.4	3.6	2.2	7	1460	70	5

[a]The uncertainty, Δv, is calculated as the standard deviation of the measurements, and n is the number of measurements.

Figure 10. Pore center growth rates as a function of pressure driving force. Three different system temperatures are used, as indicated in the legend. A growth rate measured by Hauge et al.[11] was added as a reference.
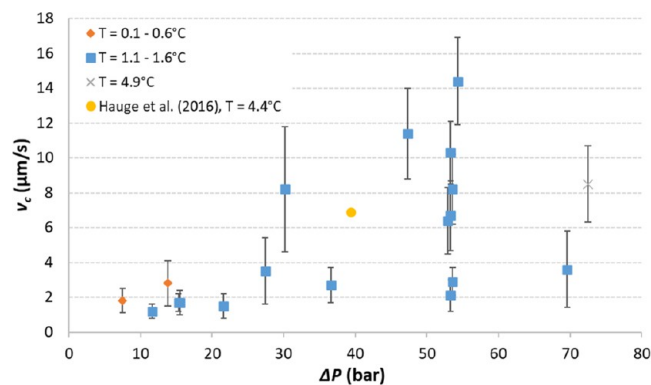
were some differences between the growth rates in each experiment, but within a single experiment, there was no significant change in the growth rate with the pore size. Some growth rates slightly increased with the pore size, while others slightly decreased with the pore size. The indifference in the pore center growth rate with the pore size in this study is probably caused by insufficient separation of the pore sizes. There was only a factor of 2 difference in the pore diameter between small and large pores. Kang et al.[18] also found a negligible effect on the CH_4 hydrate formation rate by varying the pore diameter between 6, 30, and 100 nm. The pore center growth rate was likely governed by the thickness of the water layer that was wetting the pore roof, and this water film thickness was likely constant for all pores.

3.2.2. Effect of Gas Saturation and Distribution. The variation in the pore center growth rate between experiments was investigated further by plotting the growth rate as a function of initial gas saturation in the FOV. The average value of the pore center growth rate was used for each experiment since the pore size had negligible effect on the growth rate (Table 4). Neither the pore center growth rate nor the pore wall growth rate changed significantly when the initial gas saturation varied from 0.27 to 0.52 frac. (Figure 8). The total amount of water in the FOV did not affect the hydrate growth rate along the water–gas interface. The gas distribution had no effect on the pore center growth rate. (Table 5). There was no

conclusive trend in the pore center growth rates between hydrate growth in continuous gas and isolated gas bubbles (Figure 9). Hydrate growth on an isolated gas bubble is exemplified by growth rate measurement M_5 in Figure 6. The pore wall growth rates could not be properly quantified in the isolated gas bubbles and were not included in Figure 9.

The variation in pore center growth rates between experiments at constant $P = 83-84$ bar and $T = 1.2-1.4$ °C could not be attributed to pore size, gas saturation, and gas distribution. The pore center growth rate averaged 8 ± 4 μm/s, but with outliers ranging from 2 to 14 μm/s. The average pore wall growth rate was 1228 ± 103 μm/s, which is more than 100 times faster than the pore center growth rate. This corresponds to the 2 orders of magnitude difference between the pore wall growth rate and the pore center growth rate that was found by Hauge et al.[11] and Muraoka and Yamamoto.[12] The main reason behind the discrepancy in the growth rates is
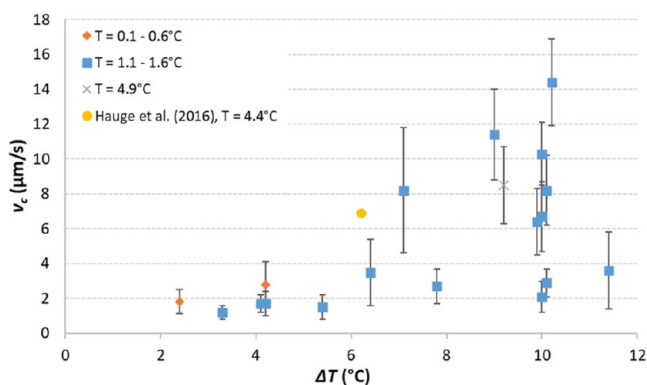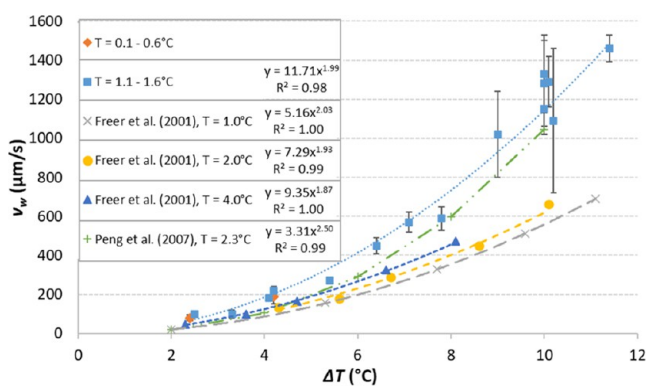
Figure 11. Pore center growth rates as a function of temperature driving force. Three different system temperatures are used as indicated in the legend. A growth rate measured by Hauge et al.[11] was added as a reference.
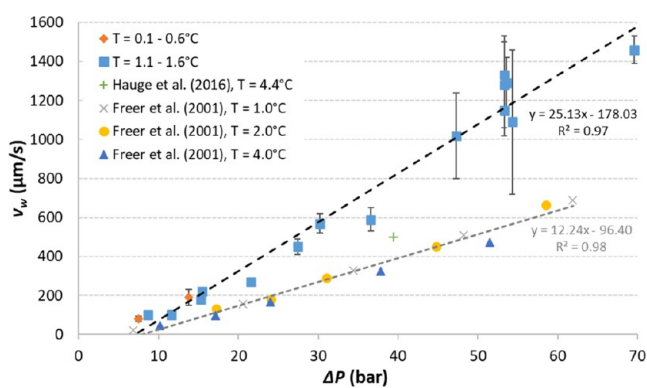
Figure 12. Pore wall growth rates as a function of pressure driving force. Two different system temperatures are used as indicated in the legend. One growth rate measured in a micromodel is included from Hauge et al.[11] as well as growth rates measured at different temperatures in a bulk system.[19]

Figure 13. Pore wall growth rates as a function of temperature driving force. Two different system temperatures are used as indicated in the legend. Data from Freer et al.[19] and Peng et al.[20] are added as references.

believed to stem from the difference in the availability of water. The hydrate crystal growth rate in water, which was observed in a few rare cases, depended on dissolved CH_4 diffusing in the water and averaged 0.3 ± 0.2 μm/s.

3.2.3. Effect of Subcooling. The pore center and pore wall growth rates for each experiment are summarized in Table 6. Five of the hydrate formations (Exp. 4.1, 7.1, 7.2, 8.1, and 8.2)

were conducted as secondary formations, meaning that the hydrate was first formed and then was dissociated by reducing the pressure below the hydrate stability pressure, before the secondary hydrate formation was triggered by repressurization. The hydrate nucleation time was significantly lower for the secondary hydrate formations, but the hydrate growth rates were unchanged compared to the primary hydrate formations. The secondary hydrate formations were therefore undertaken to reduce the experimental runtime.

The pore center growth rates were poorly correlated to the applied thermodynamic driving forces (Figures 10 and 11). The highest growth rates were measured for the highest driving forces, but a significant scatter in the results made it impossible to conclude in general. This indicated that the pore center growth rate was partly dependent on heat transfer and mass transport may be the limiting factor for the pore center growth rate in these experiments. The thin layer of liquid water that was wetting the glass plate on the top of the pores was probably limiting the pore center growth rate independent of the applied driving forces.

The pore wall growth rates were controlled by the thermodynamic driving forces and displayed a linear relationship with the applied pressure driving force, ΔP (Figure 12). The pressure driving force was calculated as the constant pressure that was used during hydrate formation minus the equilibrium pressure corresponding to the applied temperature. The linear dependency on the pressure driving force agreed with the results by Freer et al.[19] They found that the hydrate film growth rate on a planar CH_4−water interface depended linearly on the applied pressure driving force (Figure 12). However, the slope of the linear trend line in the measurements of Freer et al.[19] was approximately half of the slope of the linear trend line in the micromodel measurements. The hydrate growth rate thus seemed to be more sensitive to the applied pressure driving force in a porous medium than in a bulk system. Another trend that was common in both studies was that the hydrate growth rate increased with decreasing temperature for the same pressure driving force (Figure 12). For instance, the growth rate measured by Hauge et al.[11] at T = 4.4 °C was lower than the growth rates measured in this study at T = 1.1−1.6 °C. This trend follows naturally from the shape of the hydrate phase envelope as the hydrate equilibrium pressure becomes increasingly sensitive to the temperature as the temperature increases.

The pore wall growth rates displayed a power law dependency on the applied subcooling temperature, ΔT (Figure 13). The subcooling temperature was calculated as the equilibrium temperature corresponding to the applied pressure minus the constant temperature that was used during hydrate formation. The power law exponent was approximately equal to 2, which agreed well with the results of Freer et al.[19] (Figure 13) and Taylor et al.[3] Peng et al.[20] deduced a power law dependency where the exponent was shown to be equal to 2.5 but that equation did not fit the data in this study. The hydrate growth rate increased with increasing temperature for the same temperature driving force as highlighted by the results of Freer et al.[19] (Figure 13). This trend follows naturally from the shape of the hydrate phase envelope as the hydrate equilibrium temperature becomes increasingly sensitive to the pressure as the temperature decreases.

4. CONCLUSIONS

CH_4 hydrate growth patterns in sandstone pores were visualized and quantified using a high-pressure micromodel. The following conclusions were drawn:

- Initial hydrate formation was observed both on the gas–water interface (hydrate film) and in the liquid water phase (massive hydrate). Three hydrate growth patterns were identified: (1) Hydrate film growth along the vertical gas–water interface close to pore walls, (2) hydrate film growth along the gas–water interface toward the pore center, and (3) hydrate crystal growth in the liquid water phase fueled by dissolved CH_4.

- The hydrate crystal growth in the water phase depended on liquid diffusion and the growth rate was measured to be 0.3 ± 0.2 μm/s at $P = 83-84$ bar and $T = 1.2-1.4$ °C. The pore center growth rate and the pore wall growth rate along the gas–water interface were measured to be 8 ± 4 and 1228 ± 103 μm/s, respectively.

- The hydrate film growth rate along the gas–water interface was independent of the pore size, gas saturation, and gas distribution.

- The pore wall growth rate displayed a power law dependency on the applied subcooling temperature, ΔT. The power law exponent was found to be equal to 2. The pore center growth rate was poorly correlated to the applied thermodynamic driving forces.

■ AUTHOR INFORMATION

Corresponding Author

Stian Almenningen − *Department of Physics and Technology, University of Bergen, 5020 Bergen, Norway;* ◉ orcid.org/0000-0002-2839-8503; Email: stian.almenningen@uib.no

Authors

Maksim Lysyy − *Department of Physics and Technology, University of Bergen, 5020 Bergen, Norway*

Geir Ersland − *Department of Physics and Technology, University of Bergen, 5020 Bergen, Norway*

Complete contact information is available at:
https://pubs.acs.org/10.1021/acs.cgd.1c00396

Notes

The authors declare no competing financial interest.

■ REFERENCES

(1) Kvenvolden, K. A. Methane hydrate — A major reservoir of carbon in the shallow geosphere? *Chem. Geol.* **1988**, *71*, 41–51.

(2) Almenningen, S.; Fotland, P.; Fernø, M. A.; Ersland, G. An Experimental Investigation of Gas-Production Rates During Depressurization of Sedimentary Methane Hydrates. *SPE J.* **2019**, *24*, 522–530.

(3) Taylor, C. J.; Miller, K. T.; Koh, C. A.; Sloan, E. D. Macroscopic investigation of hydrate film growth at the hydrocarbon/water interface. *Chem. Eng. Sci.* **2007**, *62*, 6524–6533.

(4) Tanaka, R.; Sakemoto, R.; Ohmura, R. Crystal Growth of Clathrate Hydrates Formed at the Interface of Liquid Water and Gaseous Methane, Ethane, or Propane: Variations in Crystal Morphology. *Cryst. Growth Des.* **2009**, *9*, 2529–2536.

(5) Saito, K.; Kishimoto, M.; Tanaka, R.; Ohmura, R. Crystal Growth of Clathrate Hydrate at the Interface between Hydrocarbon Gas Mixture and Liquid Water. *Cryst. Growth Des.* **2011**, *11*, 295–301.

(6) Wu, R.; Kozielski, K. A.; Hartley, P. G.; May, E. F.; Boxall, J.; Maeda, N. Methane–Propane Mixed Gas Hydrate Film Growth on the Surface of Water and Luvicap EG Solutions. *Energy Fuels* **2013**, *27*, 2548–2554.

(7) Ohmura, R.; Matsuda, S.; Uchida, T.; Ebinuma, T.; Narita, H. Clathrate Hydrate Crystal Growth in Liquid Water Saturated with a Guest Substance: Observations in a Methane + Water System. *Cryst. Growth Des.* **2005**, *5*, 953–957.

(8) Li, S.-L.; Sun, C.-Y.; Liu, B.; Li, Z.-Y.; Chen, G.-J.; Sum, A. K. New Observations and Insights into the Morphology and Growth Kinetics of Hydrate Films. *Sci. Rep.* **2014**, *4*, No. 4129.

(9) Servio, P.; Englezos, P. Morphology of methane and carbon dioxide hydrates formed from water droplets. *AIChE J.* **2003**, *49*, 269–276.

(10) Clennell, M. B.; Hovland, M.; Booth, J. S.; Henry, P.; Winters, W. J. Formation of natural gas hydrates in marine sediments: 1. Conceptual model of gas hydrate growth conditioned by host sediment properties. *J. Geophys. Res.: Solid Earth* **1999**, *104*, 22985–23003.

(11) Hauge, L. P.; Gauteplass, J.; Høyland, M. D.; Ersland, G.; Kovscek, A.; Fernø, M. A. Pore-level hydrate formation mechanisms using realistic rock structures in high-pressure silicon micromodels. *Int. J. Greenhouse Gas Control* **2016**, *53*, 178–186.

(12) Muraoka, M.; Yamamoto, Y. In situ chamber built for clarifying the relationship between methane hydrate crystal morphology and gas permeability in a thin glass micromodel cell. *Rev. Sci. Instrum.* **2017**, *88*, No. 064503.

(13) Buchgraber, M.; Castanier, L. M.; Kovscek, A. R. In *Microvisual Investigation of Foam Flow in Ideal Fractures: Role of Fracture Aperture and Surface Roughness*, SPE Annual Technical Conference and Exhibition, San Antonio, Texas, USA, 2012.

(14) Almenningen, S.; Iden, E.; Fernø, M. A.; Ersland, G. Salinity Effects on Pore-Scale Methane Gas Hydrate Dissociation. *J. Geophys. Res.: Solid Earth* **2018**, *123*, 5599–5608.

(15) Pandey, J. S.; Almenningen, S.; von Solms, N.; Ersland, G. Pore-Scale Visualization of CH4 Gas Hydrate Dissociation under Permafrost Conditions. *Energy Fuels* **2021**, *35*, 1178–1196.

(16) Almenningen, S.; Flatlandsmo, J.; Fernø, M. A.; Ersland, G. Multiscale Laboratory Verification of Depressurization for Production of Sedimentary Methane Hydrates. *SPE J.* **2017**, *22*, 138–147.

(17) Chen, X.; Espinoza, D. N. Ostwald ripening changes the pore habit and spatial variability of clathrate hydrate. *Fuel* **2018**, *214*, 614–622.

(18) Kang, S.-P.; Seo, Y.; Jang, W. Kinetics of Methane and Carbon Dioxide Hydrate Formation in Silica Gel Pores. *Energy Fuels* **2009**, *23*, 3711–3715.

(19) Freer, E. M.; Sami Selim, M.; Dendy Sloan, E. Methane hydrate film growth kinetics. *Fluid Phase Equilib.* **2001**, *185*, 65–75.

(20) Peng, B. Z.; Dandekar, A.; Sun, C. Y.; Luo, H.; Ma, Q. L.; Pang, W. X.; Chen, G. J. Hydrate Film Growth on the Surface of a Gas Bubble Suspended in Water. *J. Phys. Chem. B* **2007**, *111*, 12485–12493.